Programmable transport of rotating particles in obstacle arrays

Marcos Puerto [1], Alfredo Alexander-Katz [2], Juan L. Aragones [3,4,5,*] and J. V. Alvarez [1,4,5,†]

[1] *Department of Condensed Matter Physics, Universidad Autonoma de Madrid, 28049 Madrid, Spain*

[2] *Department of Materials Science and Engineering, Massachusetts Institute of Technology, Cambridge, Massachusetts 02139, USA*

[3] *Department of Theoretical Condensed Matter Physics, Universidad Autonoma de Madrid, 28049 Madrid, Spain*

[4] *Condensed Matter Physics Center (IFIMAC), Universidad Autonoma de Madrid, 28049 Madrid, Spain*

[5] *Instituto Nicolas Cabrera, Universidad Autonoma de Madrid, 28049 Madrid, Spain*

(Received 13 February 2026; accepted 9 June 2026; published 17 July 2026)

Rotating colloids, or spinners, in obstacle arrays exhibit frequency-set stationary orbits and currents set by the competition between an inertial, Magnus-like lift and short-range attraction. Fully resolved lattice-Boltzmann simulations reveal the hydrodynamic coupling and identify the lift mechanism, while a symmetry-based Langevin model captures the resulting balance. In periodic lattices, the superposition of scalar and vector potentials produces two robust orbital regimes: corner states, in which spinners orbit individual posts, and inner states, in which orbits couple across four neighboring obstacles. Slow frequency modulation toggles these states and produce directed, stepwise transport across the grid. This establishes a minimal hydrodynamic mechanism, controlled by a single driving parameter, for programmable guidance of active rotors in structured environments.

DOI: 10.1103/c3tw-b1kw

I. INTRODUCTION

Active colloidal particles, from living organisms to synthetic beads, droplets, or microrobots, convert external or internal energy into motion. These self-driven objects can direct their motion in response to external stimuli such as chemical, mechanical, or optical cues [1–5]. When they traverse structured or crowded landscapes, the interplay between propulsion, hydrodynamic coupling, and boundary interactions gives rise to transport modes with no analog in equilibrium diffusion such as rectification [6–8], directional locking [9,10], or long-lived edge orbits [11]. Systems composed of rotating active particles, *spinners*, do not exhibit directed motion, but their activity generates azimuthal rotlet flows that significantly modify the dynamical properties of the system [12,13] and strongly influences its self-assembly [14–19]. Near boundaries, these flows couple rotation and translation, enabling spinners to glide along walls or obstacles [15,20]. In such systems, transport is determined by the environment structure, opening the door to the design of systems with programmed and/or optimized transport properties. Additionally, even in the overdamped realm of microns and milliseconds, weak but finite inertia can trigger lift forces that act on the microparticle [17,21–24], which would push it away from the boundary, while electrostatic or depletion attractions can pull it back. This balance between nondissipative effects provides dynamical control over the transport properties [25].

Here, we study the transport of rotating colloids, *spinners*, in periodic obstacle arrays. We show that the competition between inertial (Magnus-like) lift and short-range attraction generates stable orbits whose radius is set by the rotation frequency, as schematically shown in Fig. 1(a). In periodic lattices, this balance produces two robust transport modes: corner states, where particles orbit individual posts, and inner states, where orbits couple across four neighboring obstacles. Slow modulation of the rotation frequency drives reversible transitions between these modes, enabling deterministic, stepwise transport across the grid using a single control parameter. To establish this mechanism, we combine fully resolved lattice-Boltzmann (LB) simulations with a symmetry-based Langevin description that captures the effective hydrodynamic and attractive interactions. The resulting theory predicts the orbital structure and transport modes, in quantitative agreement with the simulations.

II. HYDRODYNAMIC FORCES AND LATTICE-BOLTZMANN SIMULATIONS

To quantify the hydrodynamic coupling between a spinner and an obstacle, we performed fully resolved three-dimensional LB simulations [26]. The fluid is solved on a D3Q19 lattice [27] using a multiple-relaxation-time collision operator [28] with $\Delta x = 1$ and time step $\Delta t = 1$ and setting the density of the LB fluid to $\rho_f = 1$ and its dynamic viscosity to $\eta = 1/6$. The simulation domain is $N_x \times N_y \times N_z = 128 \times 128 \times 128$, periodic in x and y and bounded in the z direction by top and bottom no-slip walls. The spinner is modeled as a sphere of radius $a = 8\Delta x$ and the obstacle as a fixed cylinder of radius $a_O = 8\Delta x$ and height $N_z \Delta x$. Both

*Contact author: juan.aragones@uam.es

†Contact author: jv.alvarez@uam.es

Published by the American Physical Society under the terms of the Creative Commons Attribution 4.0 International license. Further distribution of this work must maintain attribution to the author(s) and the published article's title, journal citation, and DOI.

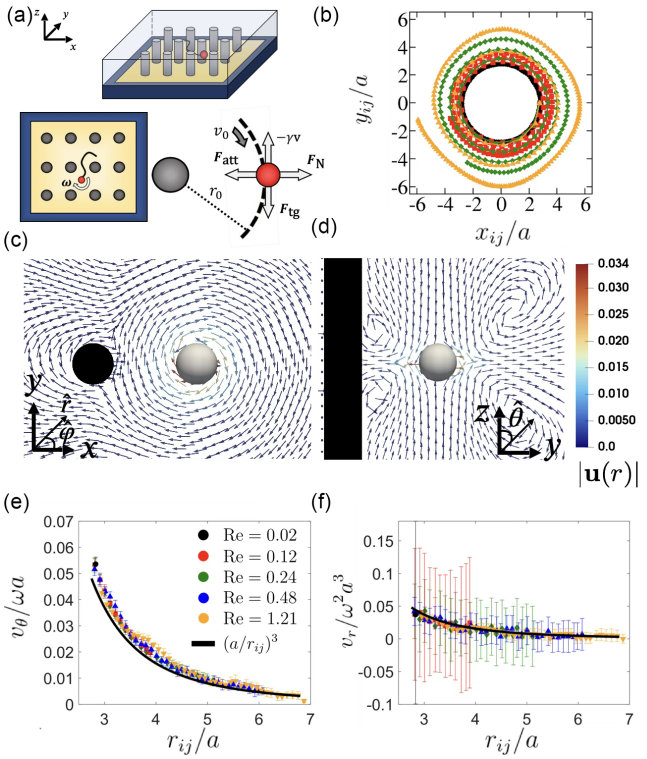

FIG. 1. (a) Perspective (top) and overhead (bottom) view of the system setup and scheme of the forces felt by the spinner. (b) Trajectories of spinning particles around a solid obstacle initially separated by $r_{ij} = 2.75a$ at Re = 0.02 (black circles), Re = 0.12 (red squares), Re = 0.24 (green diamonds), and Re = 1.21 (orange triangles). (c), (d) Fluid velocity fields on the xy and zy planes generated by the spinner at Re = 1.2 in the presence of an obstacle. (e), (f) Tangential (left) and radial (right) components of the translational velocity as a function of the distance r_{ij} between the spinner and the obstacle, along the trajectory around a solid obstacle initially separated by $r_{ij} = 2.75a$ at different rotational frequencies: Re = 0.02 (black), Re = 0.12 (red), Re = 0.24 (green), Re = 0.48 (blue), and Re = 1.21 (orange).

objects are implemented using the standard bounce-back rule [29,30], which enforces no-slip boundary conditions at their surfaces. The spinning particle is initialized at the midplane ($z = N_z/2$) and is free to move in three dimensions (3D); however, due to the vertical symmetry of the obstacle array and the absence of external vertical forces, the trajectory remains stable within the xy plane. The spinner is actuated by a time-dependent magnetic torque $\mathbf{M} \times \mathbf{B}(t)$ that imposes a prescribed angular velocity ω. This torque is applied via localized magnetic forces $\mathbf{F}_{\text{mag}}$ on surface flags attached to the spinner. Hydrodynamic forces and torques on the particle are computed through momentum exchange during bounce back. The relevant control parameter is the particle Reynolds number, $\text{Re} = \frac{\omega a^2 \rho_f}{\eta}$, which in our simulations spans $0.02 \lesssim \text{Re} \lesssim 1.2$.

A spinner in an unbounded fluid generates an azimuthal rotlet flow and exhibits no net translation. In contrast, near a boundary, rotation couples to translation via hydrodynamic interactions. To characterize this coupling, we initialize the spinner at a distance $r = 2.75a$ from a cylindrical obstacle and track its motion in the plane, resolved into radial ($\hat{r}$) and azimuthal ($\hat{\varphi}$) components relative to the obstacle center. Two dynamical regimes emerge. At low rotation rates ($\text{Re} \leqslant 0.02$), the spinner follows nearly circular orbits around the post, as shown by the black trajectory in Fig. 1(b). At higher rotation rates ($\text{Re} > 0.02$), the polar component, $\hat{\theta}$, of the flow [23], the meridional circulation in the vertical plane, generates an inertial lift that drives a slow radial migration, producing a spiral trajectory [green line in Fig. 1(b)]. The tangential velocity of the spinner, v_θ, originates from azimuthal flow scattered by the obstacle [31], which produces a secondary flow acting back on the spinner [Fig. 1(c)]. This coupling decays as $v_\theta \sim 1/r^3$ [Fig. 1(e)]. At finite Reynolds number, $\text{Re} > 0.02$, the polar component of the flow also produces a radial velocity v_r directed along $\boldsymbol{\omega} \times \mathbf{v}_\theta$ [Fig. 1(d)] [23], generating the repulsive lift. Both v_θ and v_r decay as $1/r^3$, and the lift eventually vanishes at large separations, as shown in Fig. 1(f).

III. LANGEVIN DESCRIPTION OF THE SPINNER

To describe the long-time dynamics, we coarse grain the hydrodynamic interaction with a fixed post into effective forces entering a Langevin equation. A rotating sphere generates an azimuthal rotlet flow $\mathbf{v}_f(\mathbf{r}) = (\frac{a}{r})^3 \boldsymbol{\omega} \times \mathbf{r}$, which, after scattering from the obstacle, produces a tangential hydrodynamic force on the spinner,

$$\mathbf{F}_{\text{tg}} = -\beta \frac{a^4}{r^3} \boldsymbol{\omega} \times \hat{\mathbf{r}} = \nabla \times \mathbf{c}(\mathbf{r}), \quad \mathbf{c}(\mathbf{r}) = -\beta a^4 \frac{\omega}{2r^2} \hat{\mathbf{z}}, \quad (1)$$

where β is the coupling coefficient extracted from LB simulations and $\hat{\mathbf{r}}$ is the unit vector from spinner to obstacle, $\mathbf{c}(\mathbf{r})$ is the vector potential, and $\hat{\mathbf{z}}$ is perpendicular to the substrate. At finite Reynolds number, the spinner also experiences a Magnus-like lift force, $\mathbf{F}_{\text{N}} = M_0 \boldsymbol{\omega} \times \mathbf{v}$, with $M_0 \sim \pi a^3 \rho_f$ [21] and $\boldsymbol{\omega} = \omega \hat{\mathbf{z}}$, which drives radial migration away from the obstacle. Thermal fluctuations are included through a stochastic force $\boldsymbol{\xi}(t)$ with zero mean and variance $\langle \xi_i(t) \xi_j(t') \rangle = 2 k_B T \gamma_s \delta_{ij} \delta(t - t')$, where $k_B T$ is the thermal energy and $\gamma_s = 6\pi\eta a$ is the Stokes drag coefficient of the spinner. The coarse-grained dynamics thus obey

$$m \frac{d\mathbf{v}}{dt} = \mathbf{F}_{\text{tg}}(\mathbf{r}) - (\gamma_s \mathbf{v} - M_0 \boldsymbol{\omega} \times \mathbf{v}) + \boldsymbol{\xi}(t). \quad (2)$$

Since both viscous and Magnus forces depend linearly on velocity, they combine into an effective friction matrix, $\hat{\gamma}$. In terms of the Pauli matrix σ_y, it takes the compact form $\hat{\gamma} = \gamma_s(\mathbf{I} + i\nu\sigma_y) = \hat{\mu}^{-1}$, where $\nu = \frac{\omega M_0}{\gamma_s} \approx \frac{\omega a^2 \rho_f}{6\eta} = \frac{\text{Re}}{6}$ quantifies the relative strength of Magnus to viscous forces. In steady state, the noise-averaged velocity is $\langle \mathbf{v}_j \rangle = \hat{\mu}_{jk} \langle \mathbf{F}_k \rangle$, and its azimuthal and radial components satisfy the scaling shown by the LB simulations,

$$\frac{\langle v_\theta \rangle}{\omega a} = \frac{\beta/\gamma_s}{1 + \nu^2} \left(\frac{a}{r}\right)^3, \quad \frac{\langle v_r \rangle}{\omega^2 a^3} = \frac{\rho_f}{6\eta} \frac{\beta/\gamma_s}{1 + \nu^2} \left(\frac{a}{r}\right)^3. \quad (3)$$

From our LB simulations in the low-Re regime ($\nu < 1$), we find $\beta \approx \gamma_s$, giving $v_\theta/(\omega a) \approx (a/r)^3$ and $v_r/(\omega^2 a^3) \approx (\rho_f/6\eta)(a/r)^3$, as shown in Figs. 1(e) and 1(f). Therefore, the ratio between the radial and tangential velocities scales as $\frac{\langle v_r \rangle}{\langle v_\theta \rangle} = \text{Re}/6$. Since the radial velocity is suppressed by the

factor ν at low Reynolds numbers, fluctuations that do not follow this scaling produce relative errors amplified by ν^{-1}. We observe this in our LB simulations, where numerical noise results in larger relative error bars in the radial velocity at low Re. This indicates that the susceptibility to other sources of noise, such as thermal fluctuations, will be enhanced in the radial direction and increased with the Reynolds number.

IV. TRAPPING THE SPINNER TO THE OBSTACLE

Hydrodynamic lift pushes the spinner away from the post, but this repulsion can be counteracted by an attractive short-range interaction. For simplicity, we consider a point charge Q at the obstacle center that attracts the spinner with charge q. Defining $F_a = \frac{Qq}{4\pi\varepsilon_0 a^2}$, the attractive force and its potential are

$$\mathbf{F}_{\text{att}} = -F_a\left(\frac{a}{r}\right)^2\hat{\mathbf{r}} = -\nabla u(\mathbf{r}), \quad u(\mathbf{r}) = -F_a\frac{a^2}{r}. \tag{4}$$

Balancing this attractive force with the hydrodynamic lift stabilizes the spinner on a circular orbit around the post [Fig. 1(a)]. The orbital behavior is governed only by the ratio between the attractive and viscous force, and therefore does not depend on the microscopic origin of the attraction. The long-time statistics of this bound state follow from the Fokker-Planck equation governing the probability density $\rho(\mathbf{r}, t)$,

$$\frac{\partial\rho(\mathbf{r},t)}{\partial t} = D_{\text{eff}}\nabla^2\rho - \nabla\cdot(\mathbf{W}\rho) = -\nabla\cdot\mathbf{j}, \tag{5}$$

where $D_{\text{eff}} = \frac{D}{1+\nu^2}$ is the effective diffusion coefficient arising from the combined viscous and Magnus contributions to the mobility tensor $\hat{\mu} = \hat{\gamma}^{-1}$. The drift velocity $\mathbf{W} = \hat{\mu}(\mathbf{F}_{\text{tg}} + \mathbf{F}_{\text{att}})$ combines the hydrodynamic tangential coupling and the attraction, and the conserved current is $\mathbf{j} = -D_{\text{eff}}\nabla\rho + \mathbf{W}\rho$. Because D_{eff} decreases as ν increases, the stationary probability distribution becomes narrower at higher driving frequencies, confining the spinner more tightly to its orbit.

The stationary solution follows from a Helmholtz decomposition of the drift velocity,

$$\mathbf{W} = -\nabla U(\mathbf{r}) + \nabla\times\mathbf{A}(\mathbf{r}),$$
$$U = \frac{u-\nu\mathrm{c}}{\gamma_s(1+\nu^2)}, \qquad \mathbf{A} = \frac{\mathrm{c}+\nu u}{\gamma_s(1+\nu^2)}\hat{\mathbf{z}}, \tag{6}$$

where $u(\mathbf{r})$ and $\mathbf{c} = \mathrm{c}(\mathbf{r})\hat{\mathbf{z}}$ are the Coulomb potential and hydrodynamic vector potentials defined by Eqs. (1) and (4). For a single obstacle, the stationary density and current take the exact form,

$$\rho_0(r,\omega) = \frac{1}{V_{\text{N}}}e^{-\frac{U(r)}{D_{\text{eff}}}} = \frac{1}{V_{\text{N}}}\exp\left[\frac{2E_{\text{B}}}{k_{\text{B}}T}\left(\frac{r_0}{r} - \frac{r_0^2}{2r^2}\right)\right], \tag{7}$$

$$\mathbf{j}_0(r,\omega) = -(\nabla\times\mathbf{A})\rho_0(r,\omega) = -\left(\frac{r_0}{r}\right)^3\frac{1+\frac{r}{r_0}\nu^2}{1+\nu^2}v_0\rho_0\hat{\boldsymbol{\theta}}, \tag{8}$$

where V_{N} normalizes the density and $\hat{\boldsymbol{\theta}}$ is the tangential unit vector. The characteristic orbital radius r_0, orbital velocity v_0, and binding energy E_{B} are

$$r_0 = \nu\frac{\beta\omega a}{F_a}a, \qquad v_0 = \frac{\beta}{\gamma_s}\left(\frac{a}{r_0}\right)^3\omega a, \qquad E_{\text{B}} = \frac{a}{r_0}\frac{F_a a}{2}. \tag{9}$$

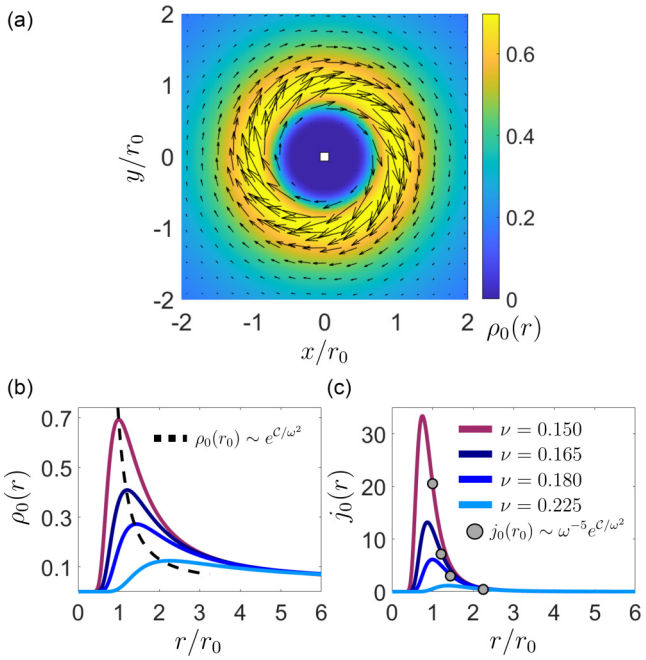

FIG. 2. (a) Normalized probability density and current density in the xy plane for the equilibrium solution, where the obstacle is located in the origin. (b) Radial profile of stationary probability density. The dashed line corresponds to the stationary density at r_0 as a function of ω. Distance values are normalized by r_0 evaluated at $\nu = 0.150$. (c) Radial profile of the stationary current. The gray dots correspond to the stationary current at the maximum density $\mathbf{j}_0(r_0)$ for different ω. Distance values are normalized by r_0 evaluated at $\nu = 0.150$.

The orbital radius grows quadratically with the rotational frequency because it is set by the balance of two different timescales of the system, $r_0 = \omega^2\tau_1\tau_2 a$, where $\tau_1 = M_0/\gamma_s$ and $\tau_2 = \beta a/F_a$, associated with inertial lift and attraction. Their ratio defines a dimensionless control parameter, $\text{Ga} = \tau_1/\tau_2 \propto F_a\rho/\eta^2$, which compares attractive and viscous forces and governs the orbital regime.

The maximum probability density lies at r_0 [Fig. 2(a)], with radial fluctuations of width $\Delta r \sim r_0\sqrt{k_{\text{B}}T/E_{\text{B}}}$. Because approaching the post is energetically costly, the density decays rapidly as $\rho_0 \sim e^{-\mathcal{C}/r^2}$, avoiding lubrication-dominated configurations. The corresponding current field $\mathbf{j}_0$ describes circular motion around the obstacle with velocity v_0, as shown in Fig. 2(c), and at the most probable radius satisfies $\mathbf{j}_0(r_0) = -v_0\rho_0\hat{\boldsymbol{\theta}}$. More generally, the current can be written as $\mathbf{j}_0(r) = -v_{\text{eff}}(r)\rho_0\hat{\boldsymbol{\theta}}$, where $v_{\text{eff}}(r) = \langle v_\theta\rangle(1+\frac{r}{r_0}\nu^2)$ combines the hydrodynamic tangential velocity [Eq. (3)] with a correction that decays as $1/r^2$. This shift explains why the maximum current is reached at a radius slightly smaller than r_0 [Fig. 2(c)]. Notably, the stationary density retains an explicit dependence on the Stokes drag γ_s, reflecting the intrinsically dissipative character of the spinner dynamics. The spinner orbital trajectory is highly controllable by frequency modulation since both r_0 and v_0 depend on rotational frequency; r_0 grows as ω^2, while the orbital velocity decays sharply as $v_0 \sim \omega^{-5}$. At sufficiently high frequencies, the spinner becomes effectively insensitive to a single obstacle, motivating the introduction

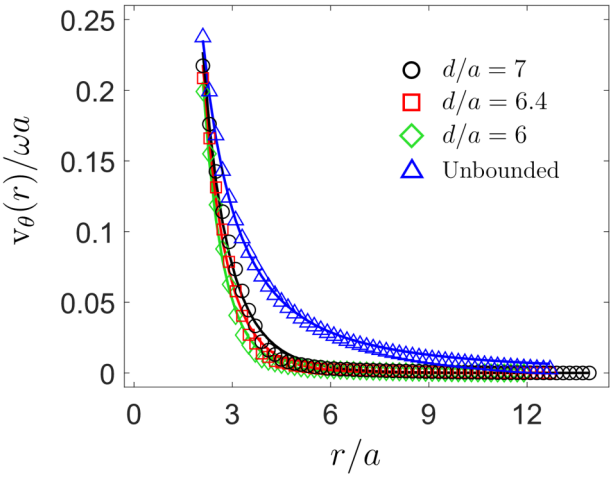

FIG. 3. Azimuthal velocity $v_\theta(r)$ generated by a sphere rotating about the z axis in a square obstacle lattice with lattice spacings $d/a = 6$ (green), 6.4 (red), and 7 (blue). Distance is normalized by the particle radius a and velocities by ωa. Solid lines show fit to the screened-rotlet form $v_\theta(r) \approx r^{-2}(1 + \frac{r}{\lambda})e^{-r/\lambda}$, with screening lengths $\lambda/a \approx 1.47$, $\lambda/a \approx 1.17$, and $\lambda/a \approx 0.96$. The unbounded rotlet results (blue triangles) follow the prediction $v_\theta \sim r^{-2}$ (blue solid line) is recovered at short distances (blue triangles), while at larger r the lattice induces an exponential cutoff.

of periodic obstacle arrays to achieve robust transport control.

V. OBSTACLE ARRAY SYSTEM

In a periodic array of obstacles the flow generated by a rotating particle experiences repeated scattering events. As a result, the long-ranged rotlet field becomes effectively screened, and its radial velocity is well described by the Brinkman fluid that decays as $v_\theta(r) \approx r^{-2}(1 + \frac{r}{\lambda})e^{-r/\lambda}$, with a lattice-dependent screening length λ measured numerically (Fig. 3) [32]. This behavior indicates that the obstacle array acts as an effective porous medium that attenuates momentum transport over distances larger than a lattice-dependent hydrodynamic screening length. Since the measured screening lengths are significantly smaller than the lattice spacing ($\lambda \ll d$), obstacle-mediated interactions are dominated by the exponential attenuation of the flow field. In the coarse-grained theory, we therefore retain only the exponential cutoff $e^{-r/\lambda}$, which captures the finite interaction range induced by hydrodynamic screening, while neglecting the algebraic prefactors of the Brinkman solution. Motivated by this observation, we incorporate screening directly into the obstacle-mediated interactions by multiplying both the scalar U and vector $\mathbf{A}$ potentials associated with each obstacle by the same exponential factor. The cutoff length is chosen to be on the order of the lattice spacing, d, ensuring that only the local obstacle environment contributes appreciably. The screened potentials are therefore written as

$$U_i = \frac{u_i - \nu c_i}{\gamma_s(1+\nu^2)} e^{-\frac{|\mathbf{r}-\mathbf{r}_i|}{d}}, \quad \mathbf{A}_i = \frac{c_i + \nu u_i}{\gamma_s(1+\nu^2)} e^{-\frac{|\mathbf{r}-\mathbf{r}_i|}{d}} \hat{\mathbf{z}}, \quad (10)$$

where r_i is the position of obstacle i. Superposing these screened contributions yields approximate expressions for the stationary density and current,

$$\rho_0(\mathbf{r}, \omega) = \frac{1}{V_N} \prod_{i=1}^{N_{obs}} \exp\left[-\frac{U_i}{D_{eff}}\right], \quad (11)$$

$$\mathbf{j}_0(\mathbf{r}, \omega) = \sum_{i=1}^{N_{obs}} (\nabla \times \mathbf{A}_i)\rho_0, \quad (12)$$

which remain in excellent agreement with numerical solutions because the two driving fields, $-\nabla U$ and $\nabla \times \mathbf{A}$, remain nearly orthogonal after superposition, so the mechanism that generates a nonequilibrium steady state persists.

Using an 8×8 square obstacle lattice, we evaluate the analytical stationary density ρ_0 for two representative rotational frequencies, $\nu = 2.0$ (left) and $\nu = 4.0$ (right) [Fig. 4(b)]. At low frequency, Coulomb attraction dominates and the spinner interacts essentially with a single post. The density consists of disconnected circular orbits, *corner states*, localized around each obstacle, and the corresponding probability current displays clockwise circulation around each post [Fig. 4(b)]. As the rotation frequency increases, hydrodynamic repulsion becomes significant and the orbital radius r_0 approaches $d/2$. Probability accumulates in the region between four neighboring obstacles, while remaining lower at the center of the unit cell, as can be seen in Fig. 4(c). In this *inner state*, the spinner forms counterrotating orbits between obstacles, although corner states and weak-current diffusion through the central region still coexist. Notice that the streamlines are independent of ν (see the Appendix). At still higher frequencies, repulsion becomes sufficiently strong that the spinner is pushed toward the center of each unit cell, as evidenced by the increased central density in Fig. 4(c). Furthermore, comparison between the analytical and numerical profiles in Fig. 4(c) demonstrates that the screened-superposition theory given by Eqs. (11) and (12) accurately captures the stationary density and current throughout this crossover.

VI. DYNAMIC CONTROL OF CORNER AND INNER TRANSPORT MODES

The spinners motion can be controlled dynamically by modulating its rotation frequency, allowing deterministic switching between corner and inner states. To demonstrate this mechanism, we track the instantaneous radius of maximum probability density, $r_{max}(t)$, while driving the spinner with a time-dependent frequency $\nu(t) = \nu_0[1 + A_0 \cos(2\pi \frac{t}{\tau_m})]$, where parameters ν_0, A_0, and τ_m are chosen so that the drive sweeps quasistatically across the corner-inner crossover. As shown in Figs. 5(a) and 5(b), $r_{max}(t)$ follows the imposed modulation, but exhibits a plateau at $r_{max} = d/2$, which originates from the structure of the stationary density. In the crossover regime, the analytic theory predicts the emergence of the inner state, in which orbits around adjacent posts hybridize to form a four-lobed trajectory running along the channels between obstacles. This inner state displays high density along the four sides of the unit cell, a robust counterclockwise circulating current, and a depleted central region. Crucially, because the inner orbit is geometrically pinned by

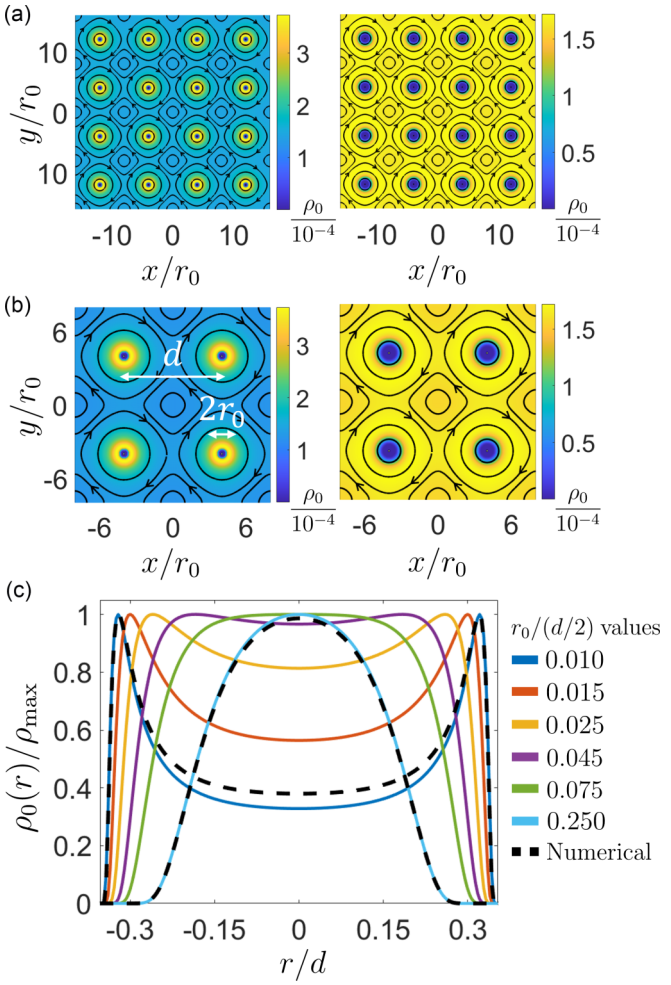

FIG. 4. (a) Normalized probability density in the xy plane, obtained from the approximate equilibrium solution for a spinner rotating at $\nu = 2.0$ (left) and $\nu = 4.0$ (right). Increasing ν enhances the hydrodynamic repulsion and shifts probability from single-post orbits to the interstitial regions between four neighboring obstacles. The streamlines of the normalized probability current are superimposed. Clockwise circulations around each obstacle correspond to *corner states*, whereas counterclockwise orbits in the channels between obstacles correspond to *inner states*. (b) Normalized probability density and current streamlines in the xy plane, obtained from the numerical solution of Eq. (5) in a 4×4 obstacle grid using a spinner's rotation frequency of $\nu = 2.0$ (left) and $\nu = 4.0$ (right). (c) Density profiles along the diagonal of the lattices unit cell at $\nu = 2.5$, which shows the crossover between corner states, found when r_0 is low compared to $d/2$, and inner states, found at higher $r_0/(d/2)$ values. The black dashed lines correspond to the numerical solutions.

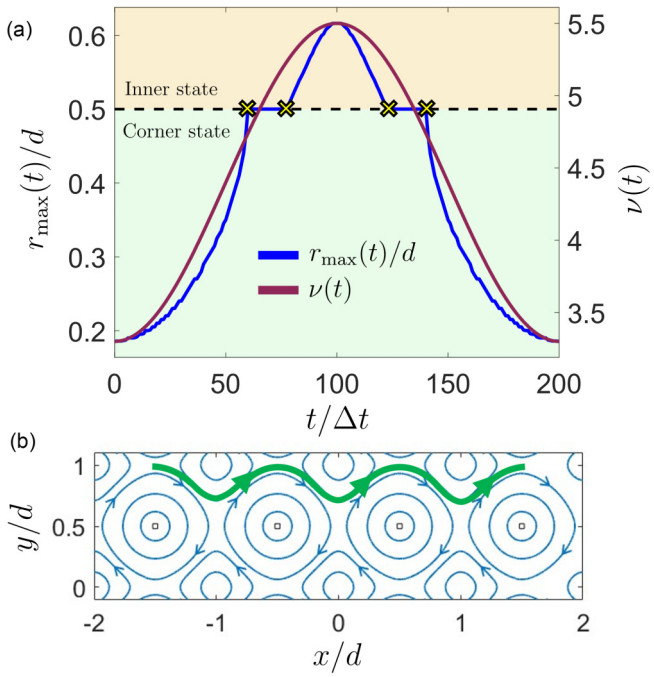

FIG. 5. (a) One period of a sinusoidal frequency modulation (purple) and the radius corresponding to maximum probability density as a function of time (blue). (b) Schematic representation of the trajectory of the particle density due to the currents.

the obstacle arrangement, its radius remains fixed at $d/2$ over a finite interval of frequencies, as can be seen in Fig. 6. The spinner remains in this pinned inner orbit until hydrodynamic repulsion becomes strong enough to push it toward the central state at higher ν. To clarify the origin of the dynamical switching mechanism, we analyze the spatial structure of the high-density regions obtained from the approximate stationary solution $\rho_0(\mathbf{r}; \nu)$ as the rotational frequency ν is varied. Figure 6 shows, for a 2×2 portion of the full lattice, the region where the density exceeds $0.99\,\rho_{\max}$ for several values of ν spanning the corner-inner crossover. At low frequencies, the attraction to each post dominates and the spinner localizes in circular orbits centered on individual obstacles. These are the corner states; the high-density region appears as four disconnected lobes, each wrapped around a single post. As ν increases, hydrodynamic repulsion becomes comparable to attraction and the orbits associated with neighboring posts begin to overlap. In this intermediate regime, the geometry of the high-density lobes reorganizes: Instead of expanding outward, the four corner orbits progressively merge along the midpoints of the edges connecting adjacent posts. Over the frequency interval $\nu \simeq 4.5$–5.25, this reorganization produces a striking effect: The position of the density maximum remains locked to the midpoint between two neighboring obstacles. The measured radius of maximum density stays fixed at $r_{\max} = d/2$, generating the plateau shown in Fig. 5(a).

This plateau arises because, in this frequency window, the most probable orbit is a geometrically constrained channel connecting neighboring posts. Increasing ν does not shift the density peak radially; instead, it broadens the corresponding lobe. The potential within the corner states is minimum until it reaches the position in between obstacles; however, the potential corresponding to the inner states is still larger, and thus, the particle density remains at that position until the repulsive potential overcomes the attractive one, as shown in Fig. 7. Once the broadened lobe feels the central region of the four-post motif, a lower-energy configuration becomes available: The spinner reorganizes into the inner state, characterized by probability maxima at the center of each four-obstacle cell and counterrotating currents. Beyond this

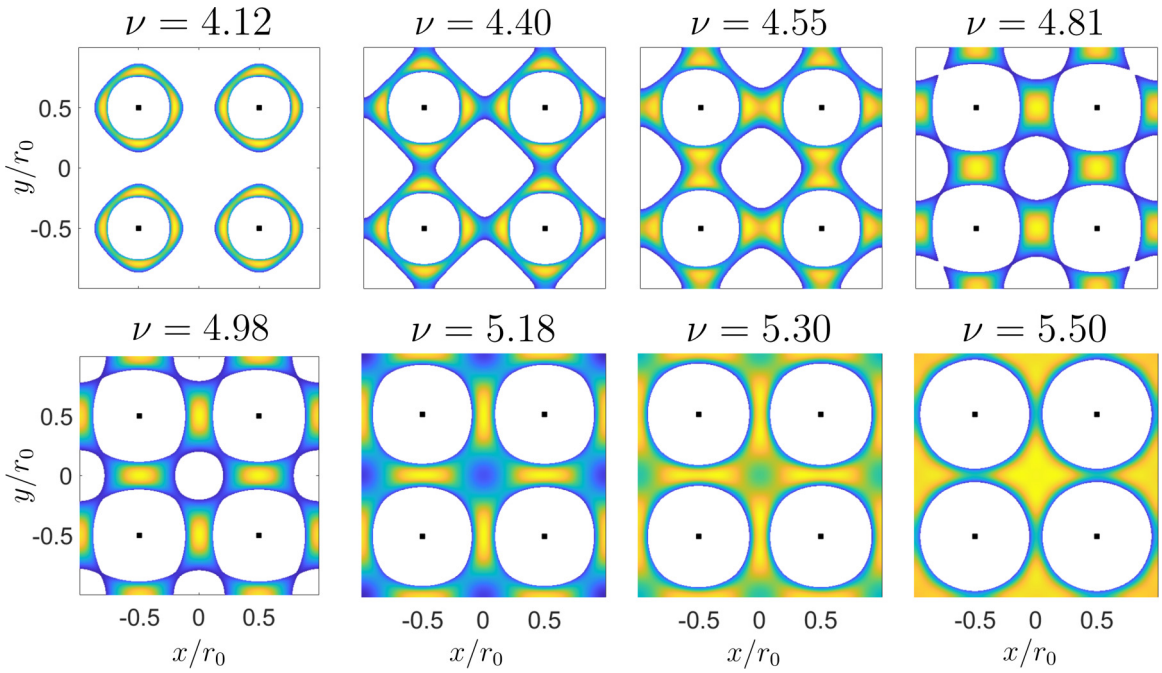

FIG. 6. Evolution of high-density regions across the corner-inner crossover. Spatial regions where $\rho_0(\mathbf{r};\nu) > 0.99\,\rho_{\max}$ for several rotational frequencies ν (increasing from left to right). At low ν, four isolated lobes appear around each obstacle (corner states). As ν increases, these lobes merge along the midpoints between obstacles, producing a frequency window where the maximal-density point remains fixed at $r_{\max} = d/2$. Upon further increase, the high-density region expands toward the centers of the four-post motifs, signaling the emergence of the inner state. This structural reorganization underlies the dynamical gateway enabling programmable transport.

point, $r_{\max}$ begins to grow again, approaching the geometric value $d/\sqrt{2}$.

This sequence of reorganizations constitutes the dynamical gateway: Slow modulation of $\nu(t)$ reliably drives the system into the plateau state $r_{\max} = d/2$, where the orbit is pinned by lattice geometry, and from which the spinner can be steered either into a corner state or into an inner state depending on the direction of frequency change. This geometric locking is what enables robust, stepwise transport in the frequency-modulated protocol.

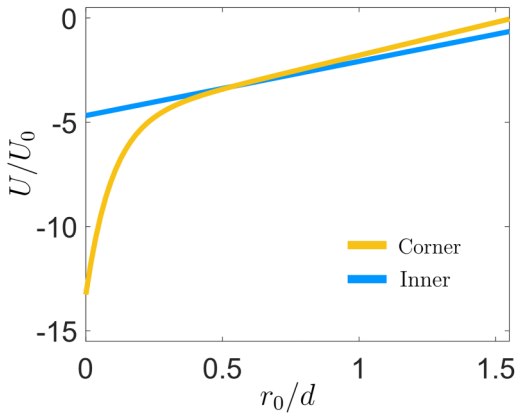

FIG. 7. Potential energy across the corner-inner crossover. Black line corresponds to the potential energy of the corner states as a function of the orbital radius. Red line corresponds to the potential energy of the inner states as a function of the orbital radius.

This plateau acts as a dynamical gateway. When the drive increases through the crossover, the spinner reliably hops into the inner state and begins counterrotating around the interstitial region. When the modulation reverses, the spinner leaves the inner orbit and returns to the $d/2$ orbit, from which it can fall back into a corner state around a different obstacle. Completing a full modulation cycle can return the spinner to its original state, but the transport becomes far more robust when the drive operates predominantly in the intermediate-frequency regime where the plateau exists. In this regime, shown in Fig. 5(b), the modulation repeatedly brings the spinner into the $r = d/2$ orbit, thereby avoiding low-frequency corner trapping and executing deterministic hops between adjacent inner orbits. Because the streamline topology is independent of ν, the transport direction and magnitude can be programmed directly through the temporal shape of $\nu(t)$. Thus, the obstacle lattice acts as a hydrodynamic mode selector, while the rotation frequency serves as a single control parameter that switches the particle between topologically distinct dynamical states, clockwise corner modes and counterclockwise inner modes. By exploiting both the robustness of the inner-orbit plateau and the opposite chirality of the two states, we obtain a simple, stable, and broadly applicable protocol for actively transporting microrotors across structured environments.

VII. CONCLUSIONS

We have shown that a single rotating colloid navigating a structured environment can be steered between distinct

hydrodynamic transport modes simply by tuning its rotation frequency. Hydrodynamic scattering, inertial lift, and a short-range attraction combine to generate robust corner and inner orbits, whose geometry and chirality are accurately captured by a coarse-grained Fokker-Planck description informed by fully resolved simulations. In periodic lattices, these modes reorganize into spatially extended steady states whose occupation can be controlled dynamically. Slow modulation of the driving frequency induces reversible transitions between the two modes and creates a finite interval where trajectories lock to the lattice geometry, enabling deterministic stepwise transport across the grid. Our results establish a minimal and predictive mechanism, controlled by the ratio between attractive and viscous forces, for programming the motion of active rotors in complex environments and open a route toward steering dense suspensions of interacting spinners using hydrodynamic design alone.

ACKNOWLEDGMENTS

The authors acknowledge financial support by MCIN/AEI/10.13039/501100011033/ for all grants listed next: J.V.A. for PID2022-139776NB-C64 supported by "ERDF A way of making Europe"; J.L.A. for PID2022-143010NB-I00 and CEX2023-001316-M, also supported by "ERDF A way of making Europe"; J.L.A. for RYC2019-028189-I and CNS2023-145447, also supported by "European Union NextGenerationEU/PRTR". A.A.-K. is grateful to MISTI Spain for funding and to the Michael and Sonja Koerner chair for financial support as well.

DATA AVAILABILITY

There are no publicly available research data or software supporting this manuscript. Requests for further information or data should be sent to the authors.

APPENDIX: INVARIANCE OF THE STREAMLINES WITH RESPECT TO ω

As shown, density current for a grid of obstacles can be written as

$$\mathbf{j}_0 = (\nabla \times \mathbf{c})\rho_0,$$
$$\mathbf{j}_0 = \frac{\rho_0}{\gamma(1+\nu^2)} \sum_i \nabla \times \left[(\mathrm{c}_i + \nu u_i) e^{-\frac{|\mathbf{r}-\mathbf{r}_i|}{d}} \hat{\mathbf{z}}\right]. \quad \text{(A1)}$$

Notice we have included the cutoff previously discussed. To calculate $\mathbf{j}_0$, we have to take the curl of both terms:

$$\nabla \times \left[(\mathrm{c}_i + \nu u_i) e^{-\frac{|\mathbf{r}-\mathbf{r}_i|}{d}} \hat{\mathbf{z}}\right] = e^{-\frac{|\mathbf{r}-\mathbf{r}_i|}{d}} \nabla \times [(\mathrm{c}_i + \nu u_i)\hat{\mathbf{z}}] + (\mathrm{c}_i + \nu u_i)\nabla \times \left(e^{-\frac{|\mathbf{r}-\mathbf{r}_i|}{d}} \hat{\mathbf{z}}\right). \quad \text{(A2)}$$

Computing both curls gives the following result:

$$\mathbf{j}_0 = -\frac{v_0 \rho_0 r_0^3}{1+\nu^2} \sum_i g_i(|\mathbf{r}-\mathbf{r}_i|)\hat{\boldsymbol{\theta}}_i,$$
$$g_i(|\mathbf{r}-\mathbf{r}_i|) = \frac{1}{|\mathbf{r}-\mathbf{r}_i|^2}\left(\frac{1+h_i}{|\mathbf{r}-\mathbf{r}_i|} + \frac{1+2h_i}{2d}\right) e^{-\frac{|\mathbf{r}-\mathbf{r}_i|}{d}}. \quad \text{(A3)}$$

We have defined $h_i = \frac{|\mathbf{r}-\mathbf{r}_i|}{r_0}\nu^2$ and $\hat{\boldsymbol{\theta}}_i = \frac{(-(y-y_i),x-x_i)}{|\mathbf{r}-\mathbf{r}_i|}$. Notice that the streamlines' direction is determined by $\sum_i g_i \hat{\boldsymbol{\theta}}_i$ and not by the factor in front that indeed depends on ω and only contributes to the current's modulus. Function g_i could depend on ω through ν^2 and r_0. However, $\nu^2 \sim \omega^2$ and $r_0 \sim \omega^2$, so the quotient ν^2/r_0 is independent of the angular frequency and so does g_i and the current's direction. This proves why it is not an issue to choose an intermediate frequency in Fig. 4(d) to represent the streamlines. It should also be said that the invariance of the streamlines with respect to the angular frequency is a property independent of the specific cutoff function used, as long as this cutoff does not depend on ω.

[1] H. Berg and E. Purcell, Physics of chemoreception, Biophys. J. **20**, 193 (1977).
[2] I. C. Fortunato, D. B. Brückner, S. Grosser, L. Rossetti, M. Bosch-Padrós, J. Trebicka, P. Roca-Cusachs, R. Sunyer, E. Hannezo, and X. Trepat, Single cell migration along and against confined haptotactic gradients, Nat. Phys. **21**, 1638 (2025).
[3] C. T. Mierke, Mechanical cues affect migration and invasion of cells from three different directions, Front. Cell Dev. Biol. **8**, 583226 (2020).
[4] C. Lozano, B. Ten Hagen, H. Löwen, and C. Bechinger, Phototaxis of synthetic microswimmers in optical landscapes, Nat. Commun. **7**, 12828 (2016).
[5] S. Koley and K. K. Nanda, Algae-like artificial organic phototactic micro-swimmers, arXiv:2308.05592.
[6] M. B. Wan, C. J. Olson Reichhardt, Z. Nussinov, and C. Reichhardt, Rectification of swimming bacteria and self-driven particle systems by arrays of asymmetric barriers, Phys. Rev. Lett. **101**, 018102 (2008).
[7] N. Nikola, A. P. Solon, Y. Kafri, M. Kardar, J. Tailleur, and R. Voituriez, Active particles with soft and curved walls: Equation of state, ratchets, and instabilities, Phys. Rev. Lett. **117**, 098001 (2016).
[8] E. Lauga, Bacterial hydrodynamics, Annu. Rev. Fluid Mech. **48**, 105 (2016).
[9] M. Brun-Cosme-Bruny, A. Förtsch, W. Zimmermann, E. Bertin, P. Peyla, and S. Rafaï, Deflection of phototactic microswimmers through obstacle arrays, Phys. Rev. Fluids **5**, 093302 (2020).
[10] C. Reichhardt and C. J. O. Reichhardt, Directional locking effects for active matter particles coupled to a periodic substrate, Phys. Rev. E **102**, 042616 (2020).
[11] S. E. Spagnolie, G. R. Moreno-Flores, D. Bartolo, and E. Lauga, Geometric capture and escape of a microswimmer colliding with an obstacle, Soft Matter **11**, 3396 (2015).
[12] J. E. Avron, Odd viscosity—Old version, J. Stat. Phys. **92**, 543 (1998).
[13] D. Banerjee, A. Souslov, A. G. Abanov, and V. Vitelli, Odd viscosity in chiral active fluids, Nat. Commun. **8**, 1573 (2017).

[14] B. A. Grzybowski and G. M. Whitesides, Dynamic aggregation of chiral spinners, Science **296**, 718 (2002).

[15] I. O. Götze and G. Gompper, Dynamic self-assembly and directed flow of rotating colloids in microchannels, Phys. Rev. E **84**, 031404 (2011).

[16] E. Climent, K. Yeo, M. R. Maxey, and G. E. Karniadakis, Dynamic self-assembly of spinning particles, J. Fluids Eng. **129**, 379 (2007).

[17] Y. Goto and H. Tanaka, Purely hydrodynamic ordering of rotating disks at a finite Reynolds number, Nat. Commun. **6**, 5994 (2015).

[18] J. L. Aragones, P. Steimel, and A. Alexander-katz, Aggregation dynamics of active rotating particles in dense passive media, Soft Matter **15**, 3929 (2019).

[19] Y. Fily, A. Baskaran, and M. C. Marchetti, Cooperative self-propulsion of active and passive rotors, Soft Matter **8**, 3002 (2012).

[20] J.-B. Gorce, K. Y. Bliokh, H. Xia, N. Francois, H. Punzmann, and M. Shats, Rolling spinners on the water surface, Sci. Adv. **7**, eabd4632 (2021).

[21] S. I. Rubinow and J. B. Keller, The transverse force on a spinning sphere moving in a viscous fluid, J. Fluid Mech. **11**, 447 (1961).

[22] P. G. Saffman, The lift on a small sphere in a slow shear flow, J. Fluid Mech. **22**, 385 (1965).

[23] J. L. Aragones, J. P. Steimel, and A. Alexander-Katz, Elasticity-induced force reversal between active spinning particles in dense passive media, Nat. Commun. **7**, 11325 (2016).

[24] X. Cao, D. Das, N. Windbacher, F. Ginot, M. Krüger, and C. Bechinger, Memory-induced Magnus effect, Nat. Phys. **19**, 1904 (2023).

[25] S. Yazdi, J. L. Aragones, J. Coulter, and A. Alexander-Katz, Metamaterials for active colloid transport, arXiv:2002.06477.

[26] B. Dünweg and A. J. C. Ladd, Lattice Boltzmann simulations of soft matter systems, in *Advanced Computer Simulation Approaches for Soft Matter Sciences III*, edited by C. Holm and K. Kremer, Advances in Polymer Science, Vol. 221 (Springer, Berlin, Heidelberg, 2008), pp. 89–166.

[27] Y. H. Qian, D. D'Humières, and P. Lallemand, Lattice BGK models for Navier-Stokes equation, Europhys. Lett. **17**, 479 (1992).

[28] D. d'Humières, Multiple-relaxation-time lattice Boltzmann models in three dimensions, Philos. Trans. R. Soc. London Ser. A **360**, 437 (2002).

[29] A. J. C. Ladd and R. Verberg, Lattice-Boltzmann simulations of particle-fluid suspensions, J. Stat. Phys. **104**, 1191 (2001).

[30] E. J. Ding and C. K. Aidun, Extension of the lattice-Boltzmann method for direct simulation of suspended particles near contact, J. Stat. Phys. **112**, 685 (2003).

[31] J. R. Blake and A. T. Chwang, Fundamental singularities of viscous flow: Part I: The image systems in the vicinity of a stationary no-slip boundary, J. Eng. Math. **8**, 23 (1974).

[32] R. Cortez, B. Cummins, K. Leiderman, and D. Varela, Computation of three-dimensional Brinkman flows using regularized methods, J. Comput. Phys. **229**, 7609 (2010).